中国光学（中英文）
Chinese Optics
核心期刊

Numerical investigation of a cavity-enhanced dual-κ DFB laser with an identical active layer for single-ended and push-pull modulation

LIU Zi-Ming, SCHATZ Richard, QIU Cheng, ZHANG Nan, CHEN Yong-Yi, QIN Li, WANG Lei, WANG Li-Jun

Citation:
LIU Zi-Ming, SCHATZ Richard, QIU Cheng, ZHANG Nan, CHEN Yong-Yi, QIN Li, WANG Lei, WANG Li-Jun. Numerical investigation of a cavity-enhanced dual-κ DFB laser with an identical active layer for single-ended and push-pull modulation[J]. *Chinese Optics*, In press. doi: 10.3724/CO.EN-2026-0007
刘子铭, Richard SCHATZ, 邱橙, 张楠, 陈泳屹, 秦莉, 王磊, 王立军. 面向单端与推挽调制的相同有源层结构双卡帕分布反馈激光器腔体增强效应的仿真研究[J]. 中国光学, 优先发表. doi: 10.3724/CO.EN-2026-0007

View online: https://doi.org/10.3724/CO.EN-2026-0007

文章编号　2097-1842(xxxx)x-0001-19

Numerical investigation of a cavity-enhanced dual-*κ* DFB laser with an identical active layer for single-ended and push-pull modulation

LIU Zi-Ming[1,2,3], SCHATZ Richard[4 *], QIU Cheng[1 *], ZHANG Nan[3 *], CHEN Yong-Yi[1,5], QIN Li[1], WANG Lei[3], WANG Li-Jun[1,3]

(1. *State Key Laboratory of Luminescence Science and Technology*, *Changchun Institute of Optics*, *Fine Mechanics and Physics*, *Chinese Academy of Sciences*, *Changchun* 130033, *China*;
2. *University of Chinese Academy of Sciences*, *Beijing* 100049, *China*;
3. *Department of Optoelectronic Information and Optical Fiber Communication*, *Pengcheng Laboratory*, *Shenzhen* 518055, *China*;
4. *Department of Applied Physics and Photonics*, *KTH Royal Institute of Technology*, *Stockholm SE*-100 *44*, *Sweden*;
5. *Jlight Semiconductor Technology Co.*, *Ltd.*, *Changchun* 130033, *China*)

* *Corresponding author*, *E-mail*: *rschatz@kth.se*; *qiucheng@ciomp.ac.cn*; *zhangn*06*@pcl.ac.cn*

Abstract: The exponential growth of large models and cloud computing is driving demand for unprecedented modulation speeds in short-reach data center links. While cavity-enhanced effects such as photon-photon resonance (PPR) and detuned loading (DL) offer a promising pathway, their practical implementation in directly modulated lasers (DMLs) often faces a critical trade-off: achieving a flat, high-bandwidth response typically requires complex fabrication techniques like butt-joint regrowth, whereas simpler identical active layer (IAL) designs suffer from uneven small-signal modulation response. In this work, we numerically investigate a dual-*κ* grating distributed feedback (DFB) laser based on an IAL structure that overcomes this trade-off. The design eliminates the need for butt-joint regrowth while effectively flattening the small-signal response. We compare its performance under single-ended and push-pull modulation schemes. The optimized laser exhibits a simulated small-signal modulation bandwidth of 185 GHz with multiple PPR peaks under single-

收稿日期: 2026-03-02; **修订日期:** xxxx-xx-xx

基金项目: 国家重点研发计划(No. 2023YFB2805100); 吉林省科技发展计划(No. SKL202402019); 国家自然科学基金(No. 62275245); 长春光机所"曙光"人才计划; 天津市科技计划项目(No. 24YFYSHZ00250); 鹏城实验室重大攻关项目; 国家重点研发计划 (No. 2024YFB29NL00100); 鹏城实验室-中国移动通信集团科技与创新基金 (No. 2024ZY2A0020); 移动信息网络国家科技重大专项(No. 2026ZD1308000)资助

Supported by the National Key R & D Program of China (No. 2023YFB2805100); the Science and Technology Development Project of Jilin Province (No. SKL202402019); the National Natural Science Foundation of China (No. 62275245); the Dawn Talent Training Program of CIOMP; the Science and Technology Project of Tianjin (No. 24YFYSHZ00250); the Major Key Project of Pengcheng Laboratory; National Key Research and Development Program of China (No. 2024YFB29NL00100); the PCL-CMCC Foundation for science and innovation (No. 2024ZY2A0020); Mobile Information Networks-National Science and Technology Major Project (No. 2026ZD1308000).

ended modulation, and a simulated small-signal modulation bandwidth of 94 GHz with suppressed low-frequency roll-off under push-pull modulation. Notably, both schemes generate clear eye diagrams at 200 Gbit/s NRZ in simulation, demonstrating their potential for ultra-high-speed operation. Furthermore, tolerance analysis confirms robustness against typical fabrication variations. The proposed IAL-based dual-κ DFB laser therefore appears to be a promising cavity-design approach for future high-speed short-reach optical interconnects. Further work is still needed to address power efficiency and practical electrical bandwidth limitations.
Key words: directly modulated laser; distributed feedback laser; single-ended modulation; push-pull modulation; photon-photon resonance effect; detuned loading effect

面向单端与推挽调制的相同有源层结构双卡帕分布反馈激光器腔体增强效应的仿真研究

刘子铭[1,2,3], Richard SCHATZ[4*], 邱 橙[1*], 张 楠[3*], 陈泳屹[1,5], 秦 莉[1], 王 磊[3], 王立军[1,3]
（1. 中国科学院长春光学精密机械与物理研究所, 特种发光科学与技术全国重点实验室, 吉林 长春 130033;
2. 中国科学院大学, 北京 100049;
3. 鹏城实验室, 光电信息与光纤通信研究部, 广东 深圳 518055;
4. 瑞典皇家理工学院, 应用物理与光子学系, 瑞典 斯德哥尔摩 SE-100 44;
5. 吉光半导体科技有限公司, 吉林 长春 130033）

摘要:随着大模型和云计算的快速发展, 数据中心短距光互连对传输速率提出了更高要求。尽管光子-光子谐振 (PPR) 效应和失谐加载 (DL) 效应为提升直接调制激光器 (DML) 带宽提供了有效途径, 但其实现通常面临结构的复杂性与调制响应的平坦性之间的权衡: 获得高带宽和较平坦的小信号响应, 往往需要对接生长等复杂工艺, 而结构较简单的相同有源层 (IAL) 设计则容易产生起伏较大的小信号调制响应。本文针对这一问题, 仿真研究了一种基于 IAL 结构的双卡帕光栅分布反馈 (DFB) 激光器。该设计无需对接生长工艺, 同时改善小信号调制响应的平坦性, 比较了其在单端调制和推挽调制两种方式下的性能。仿真表明, 优化后的器件在单端调制下可通过多个 PPR 峰实现 185 GHz 的小信号仿真带宽; 在推挽调制下可抑制低频滚降并获得 94 GHz 的小信号仿真带宽。两种调制方式在 200 Gbit/s NRZ 条件下均可得到清晰的仿真眼图, 显示出其在高速调制中的应用潜力。此外, 容差分析表明, 该结构对典型工艺偏差具有较好的鲁棒性。研究结果表明, 所提出的 IAL 结构的双卡帕光栅 DFB 激光器有望为未来短距光互连提供一种有前景的设计方案, 但其功耗及实际电带宽限制仍有待进一步研究。
关 键 词:直接调制激光器; 分布反馈激光器; 单端调制; 推挽调制; 光子-光子谐振效应; 失谐加载效应
中图分类号:TN248.4; **文献标志码:**A **doi:**10.3724/CO.EN-2026-0007 **CSTR:**32171.14.CO.EN-2026-0007

1 Introduction

The rapid evolution of optical communication technologies, coupled with advancements in computing networks, artificial intelligence, and large language models, continuously drives the demand for higher data communication capacity in data centers, necessitating increasingly higher modulation rates [1-3]. In such short-reach links, directly modulated lasers (DMLs) serve as the preferred light source due to their compact footprint, low power consumption, and cost-effectiveness. Over the years, significant efforts have been made to enhance DML bandwidth through epitaxial improvements such as introducing strain into quantum wells [4-5], optimizing doping profiles [6-7], increasing the number of quantum wells [8-9], and altering materials [10-11]. Further advancements have come from device design, including reducing the active region volume [12], optimizing grating structures [13-15], and integrating compound cavity structures [16-17]. However, these advancements are inherently limited by damping, thermal, and parasitic effects [18], which typically limit the achievable bandwidths around 30 GHz [19].

To break through this traditional bandwidth limit, several physical effects have been exploited. The detuned loading (DL) [20] effect in distributed Bragg reflector (DBR) lasers enhances differential gain by operating the laser on the long-wavelength side of the Bragg peak, where chirp-induced reflection loss changes during modulation. The photon-photon resonance (PPR) [21] effect extends bandwidth by coupling amplified side modes with modulation sidebands, creating new resonance peaks in the frequency response. Additionally, the frequency modulation-to-amplitude modulation (FM-AM) conversion effect [22] leverages the inherently higher bandwidth of frequency modulation to enhance the small-signal response. A prevalent method to engineer the PPR effect employs a butt-joint passive waveguide [23-26], but this introduces significant fabrication complexity. The identical active layer (IAL) structure was proposed to eliminate this complex regrowth step [27-31]. However, a critical shortcoming of conventional IAL-based designs is their tendency to produce non-flat, high-amplitude small-signal responses, which can degrade the quality of high-speed eye diagrams. Achieving a flat PPR response often still necessitates the complex butt-joint regrowth process [32].

Meanwhile, most PPR effect-based bandwidth enhancement research has concentrated on single-ended modulation. Push-pull modulation offers an alternative pathway to induce the PPR effect [33-35], but introduces its own challenge: it suppresses the carrier-photon resonance (CPR) peak due to a dynamic equilibrium of the average carrier density in symmetric cavity designs [36-39], creating a pronounced low-frequency roll-off that limits usable bandwidth. Mitigation strategies include using second-order grating to replace first-order grating [40-41], introducing time delays between push-pull signals [42], and adopting an asymmetric cavity with asymmetric facet coating designs [43].

To address these intertwined challenges, simplifying fabrication while achieving a flat, high-bandwidth response under both mainstream modulation schemes, we propose a novel DFB laser design based on a dual-κ grating with an IAL structure. This design intrinsically flattens the small-signal response, overcoming a key drawback of the IAL method. We then perform a systematic, comparative investigation of its performance under both single-ended and push-pull modulation.

In this work, we first describe the dual-κ DFB laser structure and its design principles for cavity enhancement. We then numerically analyze the impact of key geometric and coupling parameters on the small-signal response for each modulation scheme. Our optimized single-ended modulated laser can achieve a simulated small-signal modulation bandwidth of 185 GHz through multiple PPR peaks, while the push-pull modulated laser can reach 94 GHz in simulation by effectively mitigating the low-frequency roll-off. Both schemes generate clear eye diagrams at 200 Gbit/s NRZ in simulation. Finally, we examine the tolerance of both designs to typical fabrication variations. These results indicate the potential of the proposed laser structure for future high-speed short-reach optical interconnects.

The remainder of this paper is structured as follows: Section 2 describes the device structure and design principles. Sections 3 and 4 study the influence of key parameters on device small-signal intensity modulation response for single-ended and push-pull modulation, respectively. Section 5 presents the simulated device performance and discussion. Section 6 analyzes the impact of fabrication tolerances on yield and bandwidth. Finally, Section 7 presents our conclusion.

2 Device structure and principles of design

2.1 Device structure

Fig. 1 shows the proposed three-section dual-κ DFB laser structure. The key innovation of this structure is the use of two distinct coupling coefficients (κ) within a monolithic IAL, thereby eliminating the need for complex butt-joint regrowth. The rear-side (modulation section) and front-side grating sections (low-κ section) have a low κ-value (κ_1), whereas the central grating section (high-κ section) has a high κ-value (κ_2). All three sections share an IAL and a common Bragg wavelength of 1 310 nm. The output facet has antireflection (AR) coating, while the rear facet remains uncoated as a natural cleaved facet. The key simulation parameters are summarized in Table 1 [44].

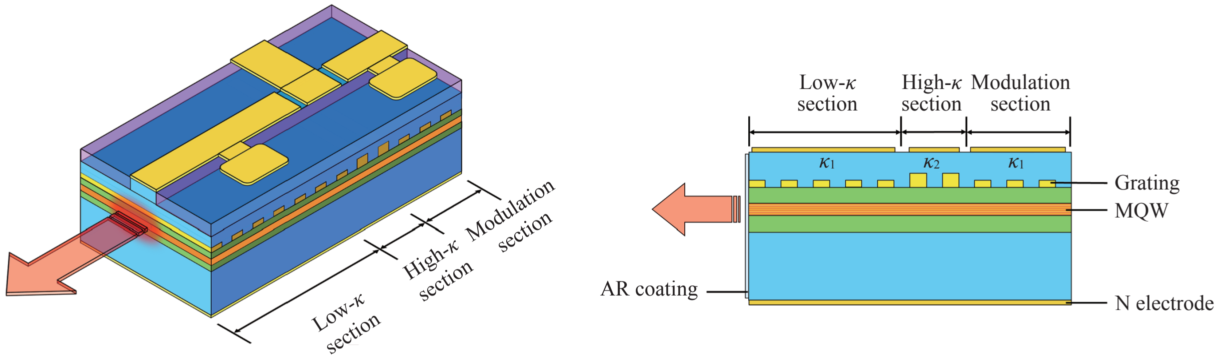

Fig. 1 (a) Schematic of dual-κ DFB laser (b) cross sectional view of the proposed laser.

Tab. 1 Simulation parameters of dual-κ DFB laser.

Parameter	Value
Length of modulation section	50 μm
Length of high-κ section	100 μm
Length of low-κ section	350 μm
Reflectivity of front (rear) facet	0 % (28.4%)
Width of active region	1.2 μm
Thickness of active layer	100 nm
Value of grating κ_1	30 cm^{-1}
Value of grating κ_2	100 cm^{-1}
Internal loss	10 cm^{-1}
Linewidth enhancement factor	4
Optical confinement factor	0.2
Effective index	3.276
Group index	3.658
Differential gain	5.0e-16 cm^{-1}
Transparency carrier density	1.5e18 cm^{-3}
Linear recombination	1.0e8 s^{-1}
Bimolecular recombination coefficient	1.5e-10 cm^3/s
Auger recombination coefficient	3.5e-29 cm^6/s

2.2 Design principles

The design principles center on engineering the cavity to effectively exploit the PPR effect for bandwidth enhancement, while maintaining an acceptably flat small-signal response. A successful PPR effect requires participating side modes to exhibit sufficient response strength above the −3 dB level and to be closely spaced in frequency relative to the CPR peak [45]. In this design, the cavity length of the modulation section is shortened to raise the fundamental CPR frequency.

The magnitude of reactive energy U for each mode, defined by the depth of the standing wave pattern, as described by Equation (10) in the Appendix, is a key factor for high-speed modulation. Reactive energy concentrated within the modulated section directly supports the modulation response. Near the AR-coated front facet, the energy is primarily in the traveling wave form, as shown in Fig. 2(a), which does not directly contribute to high-speed modulation [46]. Although traveling wave energy V increases with the total photon energy S, the reactive energy remains weak in this facet.

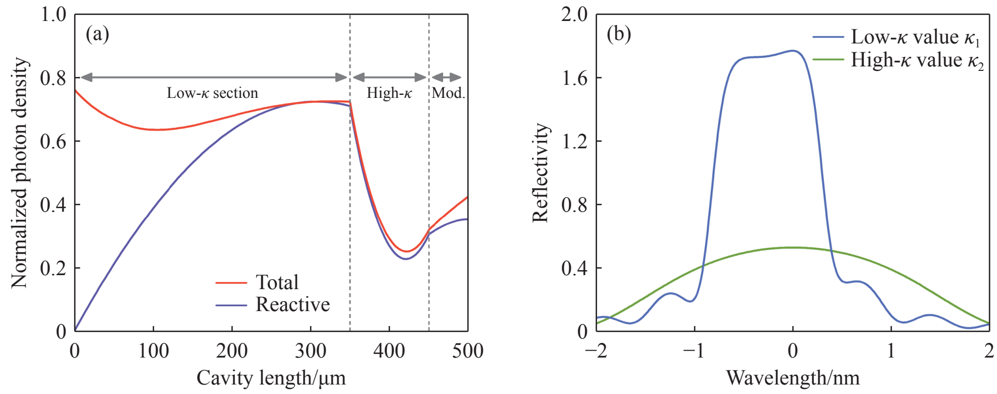

Fig. 2 (a) Distribution profile of main mode total and reactive photon densities in laser cavity (b) the reflection profile for low κ-value κ_1 and high κ-value κ_2.

The dual-κ grating is designed to tailor this energy distribution and the cavity's reflection spectrum. A high κ_2-value combined with a short high-κ section produces a relatively wide reflection peak. This configuration enhances the confinement of reactive energy inside the modulation section of the cavity. Conversely, a low κ_1-value combined with a long low-κ section generates a narrow reflection peak with a steep slope, as shown in Fig. 2(b). This sharp spectral feature promotes a high side-mode suppression ratio (SMSR) and enhances the DL effect by providing a strong wavelength-dependent loss.

Both single-ended and push-pull modulation schemes are implemented and optimized using the same dual-κ DFB structural platform. For single-ended modulation, the central high-κ section is left unpumped. For push-pull modulation, the same section is electrically biased to store additional photon energy, which alters the dynamic interaction between the modulated sections [47]. We adopt the LaserMatrix software for laser simulations, and previous studies using this software [48-52] have demonstrated its maturity and effectiveness for simulations. The bandwidth values reported in this work correspond to the simulated small-signal modulation response obtained from the simulation model. In practical devices, the usable bandwidth will also be limited by the finite electrical bandwidth of the electrode, pad, interconnect, package, and driver. Further details of the simulation model are provided in the Appendix.

3 Dependence of device parameters on modulation bandwidth in single-ended modulation

This section investigates the influence of key structural parameters on the small-signal modulation response under single-ended operation. The analysis focuses on the length of the low-κ section and the coupling coefficient (κ_2) and length of the high-κ section. The objective is to understand how these parameters govern the PPR frequencies and amplitudes, thereby determining the overall bandwidth and flatness of the response. Throughout this analysis, the currents of the modulation and low-κ sections are fixed at 25 mA and 175 mA, respectively, while the κ_1-value for both sections remains constant at 30 cm^{-1}. These bias conditions are chosen to optimize the cavity-enhanced modulation response and to make the PPR-related behavior clear, rather than to minimize the total power consumption.

The length of the low-κ section primarily influences the PPR resonance frequency as a key component of the compound cavity for introducing the PPR effect. As illustrated in Fig. 3, an increase in the length of the low-κ section leads to a reduction in the PPR frequency. The relaxation oscillation frequency remains unchanged, which is attributed to the fixed length of the modulation section. However, mode hopping and unstable operation are observed when the cavity length approaches 400 μm. Therefore, a low-κ section length of 350 μm is selected for subsequent optimization, providing a stable operating point with a suitable PPR frequency.

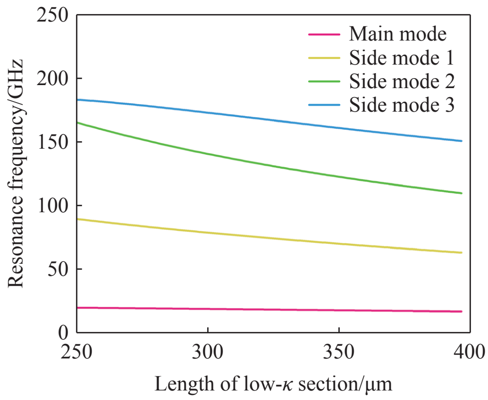

Fig. 3 Resonance frequencies of different laser modes at low-κ section lengths from 250 to 400 μm.

3.1 Dependence of modulation bandwidth on the κ_2-value of high-κ section

With the cavity length fixed, the coupling coefficient of the high-κ section, κ_2, is varied to analyze its effect on the small-signal response. As shown in Fig. 4, for 80 and 90 cm^{-1}, four response peaks cause a large bandwidth enhancement. At higher κ_2-value, the fourth peak shifts toward higher frequencies and no longer contributes to bandwidth extension, while the frequency intervals between the remaining peaks become smaller.

This increase in the κ_2-value enhances the coupling between modes and changes the loss of each mode, while also strengthening the CPR response. Consequently, the first two PPR modes on the long-wavelength side gradually move closer to the CPR peak. Meanwhile, the response intensity of the fourth resonance peak on the short-wavelength side progressively weakens due to increased loss and shifts away from the CPR peak, resulting in a roll-off below −3 dB.

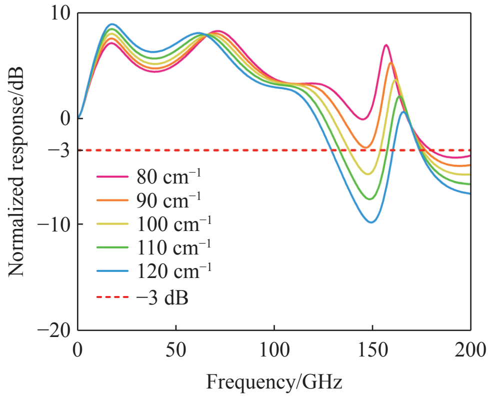

Fig. 4 Normalized single-ended modulation response at κ_2-values of high-κ section from 80 to 120 cm^{-1}.

3.2 Dependence of modulation bandwidth on the length of high-κ section

The length of the high-κ section is another critical parameter affecting the PPR characteristics. Fig. 5 shows the dependence of the small-signal intensity modulation response on the high-κ section length varying from 50 to 150 μm. Three PPR peaks appear for lengths of 50 and 75 μm, where the second PPR peak is caused by the merged responses of the side modes on both sides of the main mode. Increasing the length reduces the PPR peak frequencies, isolates the third peak, and suppresses its contribution to bandwidth enhancement.

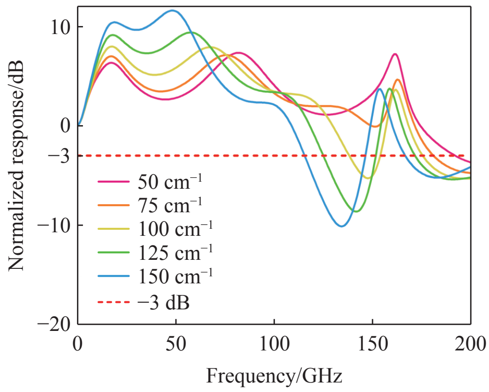

Fig. 5 Normalized single-ended modulation response at high-κ section lengths from 50 to 150 μm.

Similar to the trend observed for κ_2-values, the third PPR peak that exhibits roll-off is located on the short-wavelength side of the main mode. The slope of this grating section's reflection peak changes significantly with length, and the frequency variation of the side mode is more pronounced, since the mode spacing is directly affected by the complex-cavity length. Although increasing the length reduces the frequency interval between the long-wavelength PPR modes and the main mode, it also makes the small-signal response intensity more pronounced, which is detrimental to large-signal modulation.

In summary, the parametric analysis reveals clear design trade-offs. A lower κ_2-value strengthens the response peaks, whereas a shorter cavity length increases the frequency separation from the main mode and reduces the peak intensity. Therefore, the optimal strategy involves utilizing shorter cavity lengths to control the amplitude effectively, combined with higher κ_2-values to reduce the frequency interval, thereby enhancing the overall performance.

4 Dependence of device parameters on modulation bandwidth in push-pull modulation

This section presents a systematic analysis of the push-pull modulation scheme implemented on the same dual-κ DFB structure. In contrast to single-ended modulation, push-pull modulation applies equal-magnitude but opposite-phase modulation currents. In a symmetrical laser cavity, this means the gain increase in one section is offset by an equal decrease in the other. Consequently, the round-trip gain (RTG) of the entire cavity maintains dynamic balance during modulation, leaving the average carrier concentration and average refractive index unchanged. This suppresses the CPR peak by avoiding net periodic perturbation to the RTG. As a result, the frequency response often falls below −3 dB before the PPR enhancement becomes effective. Our design employs an asymmetric cavity to mitigate this issue.

The following analysis examines how key parameters influence the small-signal response, with the goal of minimizing roll-off and maximizing bandwidth. Throughout this analysis, the following parameters are fixed: the modulation and low-κ sections currents at 25 mA and 175 mA, respectively; the κ_1-value at 30 cm^{-1} for both sections; and the high-κ section length at 100 μm. The central high-κ section is biased at 80 mA to store greater photon energy [47]. This additional DC bias helps reduce the low-frequency roll-off, but it also increases the static power consumption and thermal load.

The choice of which sections are driven as the push-pull pair fundamentally affects the modulation characteristics.

Fig. 6 compares the small-signal responses when push-pull modulation is applied between the modulation (rear) section and either the high-κ (middle) or low-κ (front) sections. Modulation with the middle section produces a higher CPR response intensity, attributed to stronger reactive energy confinement by the higher κ_2-value, which increases carrier concentration sensitivity and enhances the side-mode response peak. In contrast, modulation with the front section yields a relatively flat response. Therefore, to ensure good eye-diagram quality, the rear modulation section and the front low-κ section are selected as the push-pull pair for subsequent optimization.

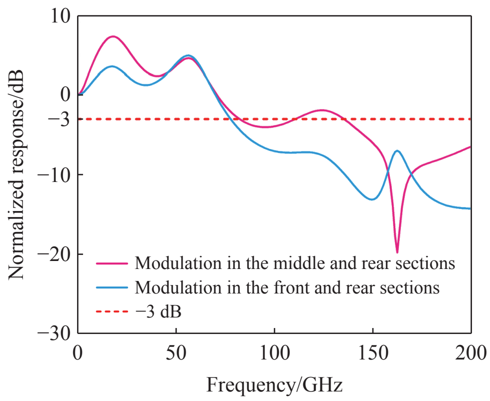

Fig. 6　Normalized push-pull modulation response in the modulation (rear) section combined with high-κ (middle) and low-κ (front) sections, respectively.

4.1　Dependence of modulation bandwidth on the κ_2-value of high-κ section

With the push-pull pair established, we first investigate the role of the high-κ section's coupling coefficient. A high κ_2-value provides strong coupling between laser modes and pronounced photon energy confinement. With the high-κ section biased at 80 mA, Fig. 7 shows the dependence of the small-signal response on the κ_2-value.

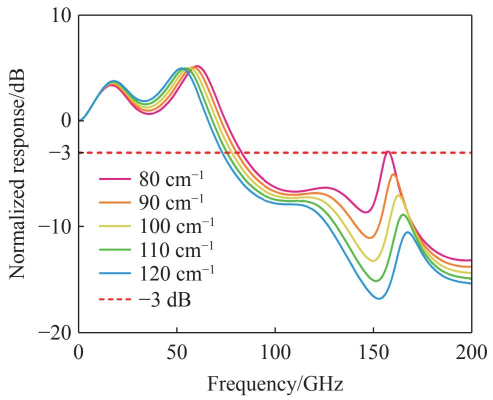

Fig. 7 Normalized push-pull modulation response at κ_2-values of high-κ section from 80 to 120 cm^{-1}.

Under push-pull modulation, only one side mode contributes to the PPR effect for bandwidth extension. As the κ_2-value increases, the CPR frequency remains fixed, while the first PPR peak shifts toward it, reducing the bandwidth. Two additional response peaks below the −3 dB level are observed: one on the long-wavelength side follows the same trend as the PPR peak above with κ_2-value, while the other, on the short-wavelength side, exhibits the opposite behavior.

This behavior resembles that in single-ended modulation, where increasing the κ_2-value alters the side modes loss, particularly for the short-wavelength mode. Based on this, a κ_2-value of 100 cm^{-1} is selected and kept constant for the following analysis.

4.2 Dependence of modulation bandwidth on the length of low-κ section

Unlike single-ended modulation, a primary challenge in push-pull modulation is mitigating the low-frequency roll-off between the CPR and PPR peaks. The length of the low-κ section, which is part of the push-pull pair, is a critical parameter for addressing this. With the low-κ section fixed at 175 mA, Fig. 8 shows that varying its length from 200 to 400 μm substantially alters the bandwidth. A length of 200 μm yields a bandwidth of 100 GHz but with a pronounced roll-off, primarily due to the high DC bias on this section. This indicates that reducing the bias current could mitigate this suppression. As the length increases, the PPR frequency gradually decreases from 80 GHz at 200 μm to 51 GHz at 400 μm, while its response intensity strengthens. Thus, to achieve a flat small-signal response, a shorter low-κ section is preferable, provided the DC bias is also reduced accordingly to prevent excessive roll-off.

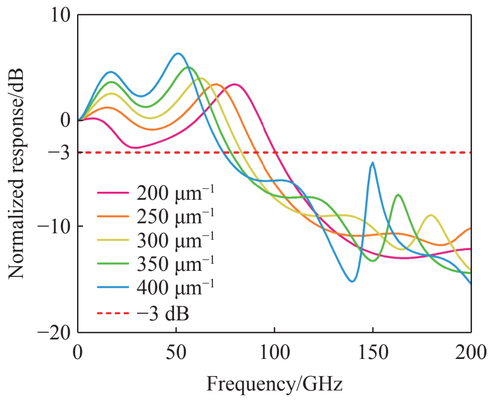

Fig. 8 Normalized push-pull modulation response at low-κ section lengths from 200 to 400 μm.

In summary, the parametric study for push-pull modulation confirms that the asymmetric cavity design successfully addresses the characteristic CPR roll-off problem. The small-signal response shows limited dependence on the κ_2-value, and a higher DC bias in the high-κ section contributes stability. The key to achieving a flatter response is to select a shorter low-κ section and reduce its bias current, so as to balance the PPR strength against low-frequency suppression.

5 Simulated device performance and discussion

This section presents the simulated steady-state and dynamic performance of the optimized laser designs for both single-ended and push-pull modulation, based on the parametric analysis conducted in Sections 3 and 4. The results are compared against the initial dual-κ structure and a conventional single-κ grating reference laser, where κ_2-value was uniformly replaced by κ_1-value while keeping all other parameters identical, thus highlighting the performance improvements enabled by the optimized dual-κ design.

5.1 Device performance of single-ended modulation laser

The optimized parameters for the single-ended modulation laser are summarized in Table 2. Performance was evaluated through the steady-state RTG, lasing spectrum, small-signal modulation response, and large-signal eye diagrams.

Tab. 2　Optimized parameters of single-ended modulation laser.

Parameter	Value
Length of high-κ section	50 μm
Value of grating κ_2	120 cm^{-1}

The steady-state analysis confirms the intended multi-mode interaction. The RTG spectrum in Fig. 9 shows three side modes participating in the PPR effect, which is crucial for broadband enhancement. The corresponding lasing spectrum in Fig. 10 reveals these side modes are separated from the main mode by 0.46 nm and 0.88 nm (long-wavelength side) and 0.94 nm (short-wavelength side). The small-signal response in Fig. 11 shows distinct PPR peaks at frequencies proportional to these wavelength separations. Because the short-wavelength and the second long-wavelength side modes have similar interval values, their corresponding PPR peaks partially overlap, appearing together as the third resonance peak. The optimized design achieves a simulated −3 dB small-signal modulation bandwidth of 185 GHz, which is significantly higher than that of both the initial structure and the single-κ reference, while also showing a flatter response.

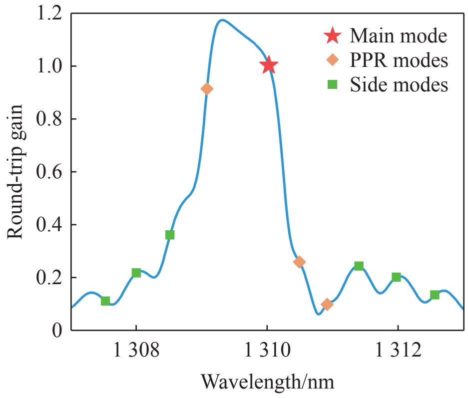

Fig. 9　Round-trip gain and lasing mode of the optimized laser for single-ended modulation.

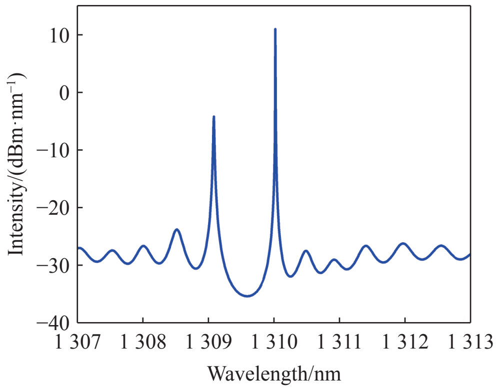

Fig. 10　Lasing spectrum of the optimized laser for single-ended modulation.

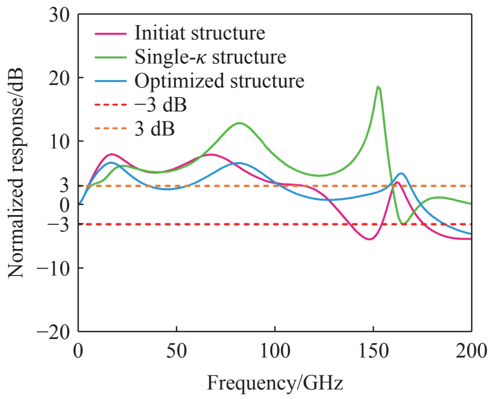

Fig. 11　Normalized modulation response of three structures for single-ended modulation.

Eye diagrams were simulated under a modulation current swing of 10-40 mA at 200 Gbit/s NRZ. The initial structure laser exhibits a blurred eye diagram, as shown in Fig. 12(a); the single-κ grating structure laser shows an almost closed eye in Fig. 12(b), while the optimized structure laser displays a clearly open eye in Fig. 12(c).

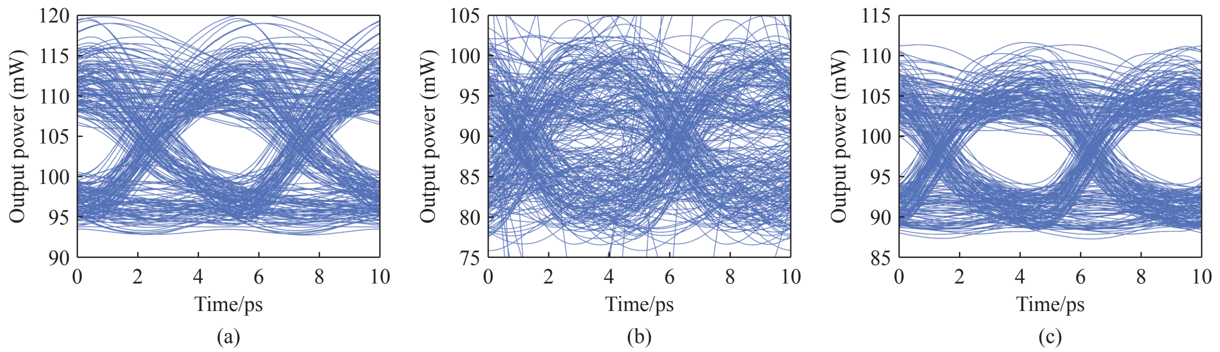

Fig. 12 Eye diagrams for single-ended modulation in (a) initial laser (b) single-κ grating laser and (c) optimized laser structures.

5.2 Device performance of push-pull modulation laser

The optimized parameters for the push-pull modulation laser are listed in the Table 3. Following the same evaluation procedure, steady-state RTG and lasing spectrum were obtained, and dynamic responses were compared with the initial structure and a single-κ laser.

Tab. 3 Optimized parameters of push-pull modulation laser.

Parameter	Value
Length of low-κ section	200 μm
Current of high-κ section	80 mA
Modulation regions	modulation (rear) and low-κ (front) sections

The operating principle under push-pull modulation differs significantly. The RTG spectrum in Fig. 13 indicates that only one side mode on the long-wavelength side, separated by 0.47 nm (Fig. 14), contributes dominantly to the PPR effect. Consequently, the small-signal response in Fig. 15 exhibits a single dominant PPR peak above −3 dB. While the initial structure shows a higher response magnitude and the single-κ reference suffers from severe roll-off, the optimized asymmetric design achieves a flatter simulated response profile, resulting in a simulated small-signal modulation bandwidth of 94 GHz.

The 200 Gbit/s NRZ eye diagrams under push-pull modulation are shown in Fig. 16. The optimized laser Fig. 16(c) produces a clearly open eye in simulation. The initial structure Fig. 16(a) shows a blurred eye due to an uneven frequency response, and the single-κ reference Fig. 16(b) exhibits a nearly closed eye due to its limited bandwidth. Notably, the push-pull scheme yields a higher extinction ratio than the single-ended case, which is advantageous for signal detection.

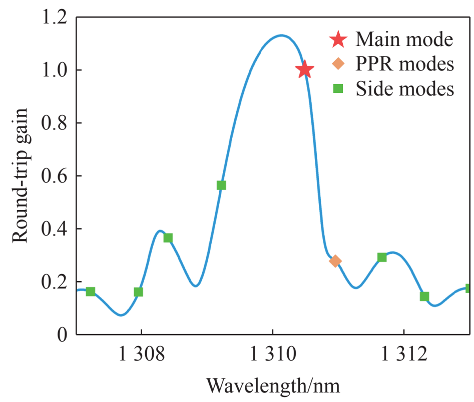

Fig. 13 Round-trip gain and lasing mode of the optimized laser for push-pull modulation.

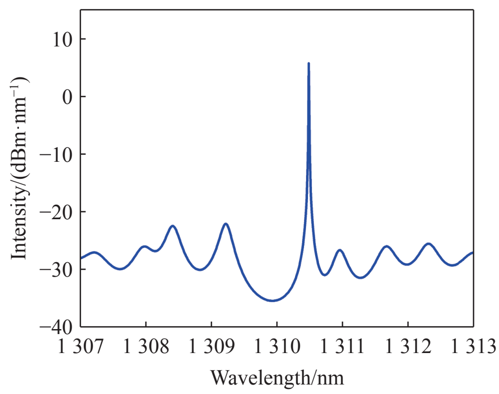

Fig. 14 Lasing spectrum of the optimized laser for push-pull modulation.

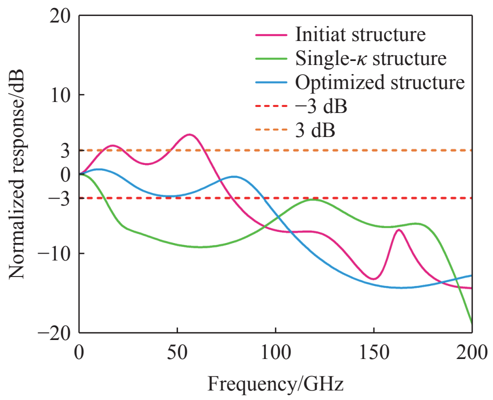

Fig. 15　Normalized modulation response of three structures for push-pull modulation.

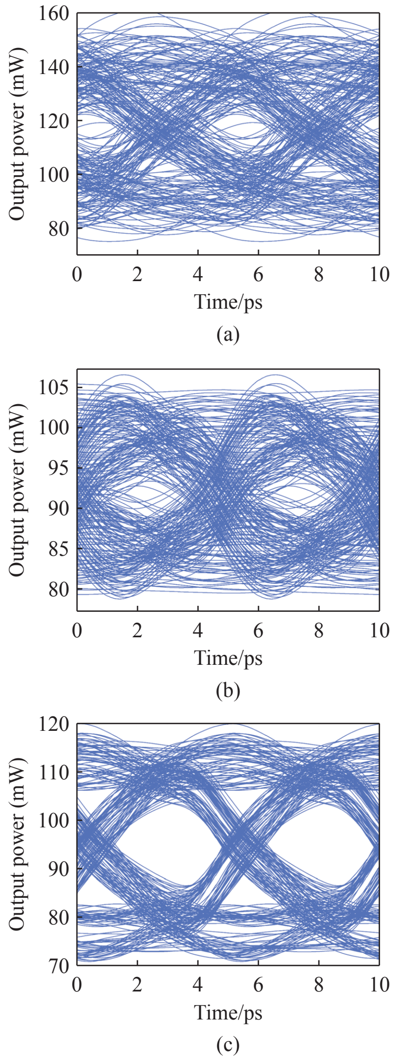

Fig. 16　Eye diagrams for push-pull modulation in (a) initial laser (b) single-κ grating laser and (c) optimized laser structures.

5.3　Discussion

The two modulation schemes show different advantages. Under single-ended modulation, the optimized laser reaches a simulated small-signal modulation bandwidth of 185 GHz by making use of multiple PPR peaks, and the driving scheme is relatively simple. Under push-pull modulation, the simulated bandwidth is lower at 94 GHz, but the eye diagram is cleaner and the extinction ratio is higher. This mainly comes from the asymmetric cavity design, which helps reduce the low-frequency roll-off in the push-pull case. These results suggest that the same dual-κ IAL structure can be adapted for different modulation requirements.

It should also be noted that the optimized bias conditions used here are relatively high for short-reach interconnect applications, where power efficiency is important. In the single-ended case, the modulation and low-κ sections are biased at 25 mA and 175 mA, respectively. In the push-pull case, an additional 80 mA bias is applied to the central high-κ section. These bias settings are selected mainly to improve the modulation response, rather than to reduce power consumption. The additional bias in the push-pull design helps store more photon energy and alleviates the low-frequency roll-off, but it also increases static heating.

Self-heating may affect the refractive index, differential gain, and carrier recombination, and may therefore shift the PPR peak positions and alter the relative peak amplitudes. It may also influence carrier transport and further affect the usable modulation response. A quantitative thermal analysis is not included here because reliable thermal simulation in LaserMatrix requires experimentally calibrated temperature-dependent material parameters, together with realistic electrical and thermal resistance values for the specific device. Since these inputs are not available at present, the discussion here is limited to the physical implications of the bias conditions.

In practical devices, the final electro-optic bandwidth will also be limited by the electrical response of the electrode, pad, interconnect, package, and driver. To illustrate this effect, the small-signal response is further evaluated together with an equivalent first-order external low-pass response. This treatment is not intended to reproduce the full electrical parasitic effects of a specific device layout. Instead, it is used here as a simple and consistent way to examine how finite external electrical bandwidth would compress the small-signal response predicted by the optical simulation.

Fig. 17 shows the corresponding results for several representative levels of external electrical limitation, with the low-pass frequencies set to 0.5 and 0.75 times the bandwidth, ranging from relatively weak limitation to more pronounced limitation. In the single-ended case, the external electrical roll-off reduces the available bandwidth, but the multiple PPR peaks still provide partial equalization of the roll-off and help maintain a relatively broad response. In the push-pull case, the response is dominated by a single high-frequency enhancement, which is weakened noticeably, so the response falls below the −3 dB level at a lower frequency.

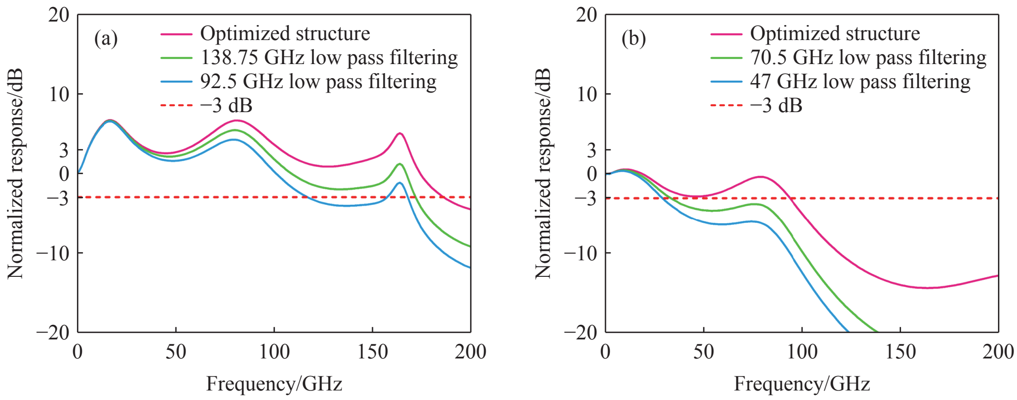

Fig. 17 Effect of an equivalent first-order external electrical low-pass limitation on the optimized small-signal responses: (a) single-ended modulation and (b) push-pull modulation.

In practice, these results indicate that the experimentally achievable bandwidth will depend not only on the cavity design itself, but also on whether the external electrical path is fast enough to preserve the PPR-assisted response. In this sense, the single-ended modulation is more tolerant of external electrical roll-off because of its multiple PPR peaks, whereas the push-pull modulation is more directly constrained by finite external electrical bandwidth. Therefore, further improvement of the experimentally achievable bandwidth will require not only cavity optimization, but also co-design of the electrode, interconnect, package, and driver.

6 Device fabrication tolerances

To assess the practical feasibility of the proposed designs, this section analyzes the impact of fabrication variations on laser yield and bandwidth stability. The analysis focuses on three key variation sources: random back-facet phase, deviations in grating coupling coefficients (κ), and variations in section lengths.

6.1 Device fabrication tolerances of single-ended modulation laser

The single-mode yield was evaluated by defining a SMSR > 30 dB across a random back-facet phase variation from 0° to 360°. The design yields a single-mode yield of approximately 77%, as shown in Fig. 18, indicating good robustness against this common phase uncertainty.

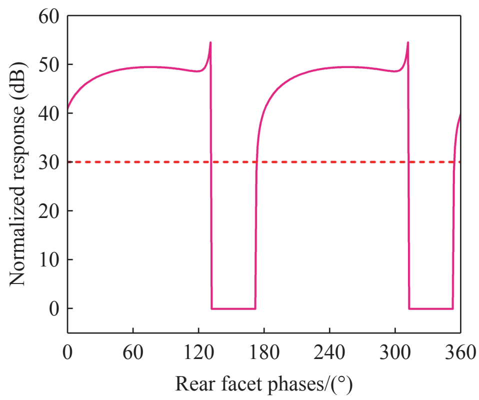

Fig. 18 Effect of random back-facet phase on the single-mode yield for single-ended modulation laser.

The impact of κ and length variations on the −3 dB bandwidth was quantified. The κ_1-and κ_2-values across the three sections were varied within an error range of ± 5 cm^{-1}. The resulting bandwidth variation is about 10 GHz for κ_1-values and 0.6 GHz for κ_2-values (Fig. 19). Similarly, length variations of ± 10 μm in the low-κ and modulation sections cause bandwidth changes of 8 GHz and 4 GHz, respectively (Fig. 20). These results indicate that parameters of the low-κ section have a more pronounced influence on bandwidth, as they directly affect the frequency and strength of the PPR peak.

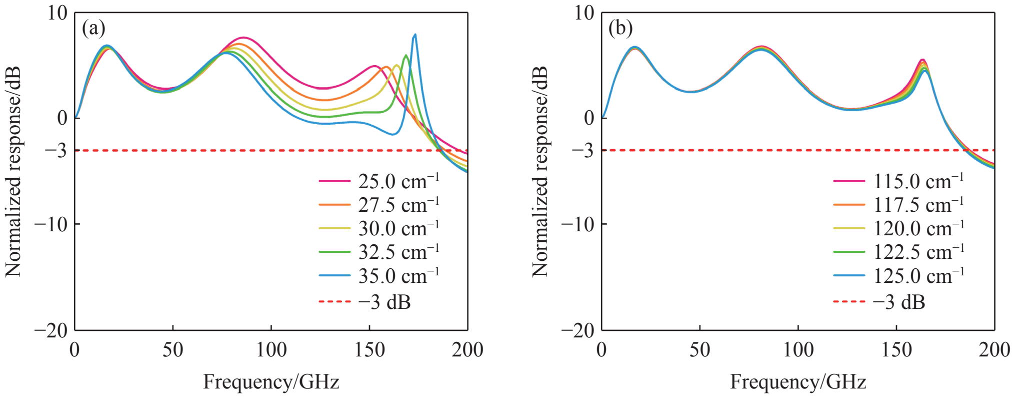

Fig. 19　Effect of fabrication variations on the small-signal response of the optimized single-ended modulation laser: (a) the κ_1-value of the low-κ and modulation sections and (b) the κ_2-value of the high-κ section.

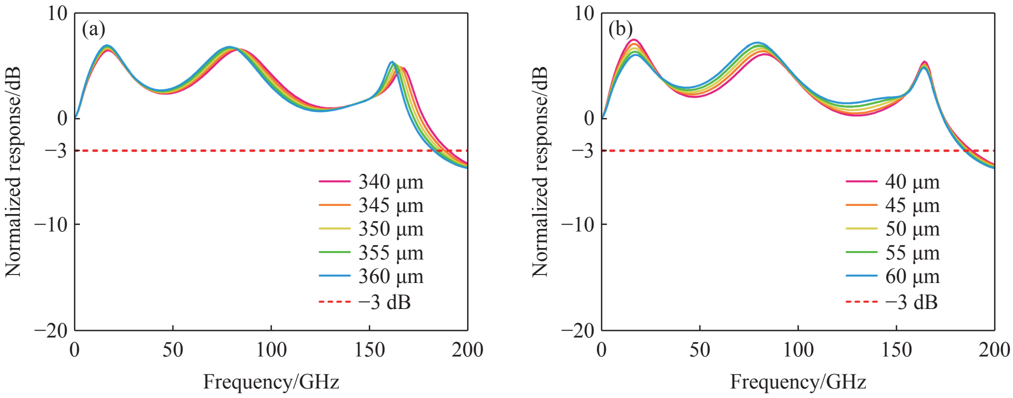

Fig. 20　Effect of fabrication variations on the small-signal response of the optimized single-ended modulation laser: (a) the length of the low-κ section and (b) the length of the modulation section.

6.2　Device fabrication tolerances of push-pull modulation laser

The same tolerance analysis was applied to the push-pull design. This design shows an even higher single-mode yield of approximately 93% over the same back-facet phase range, as shown in Fig. 21, suggesting enhanced mode stability under the push-pull operating condition.

Variations in κ and length have a more subdued effect on bandwidth in this scheme. As shown in Fig. 22, bandwidth variations are 4 GHz and 3.5 GHz for changes in κ_1-and κ_2-values, respectively. Fig. 23 indicates the length variations of ±10 μm in the low-κ and modulation sections cause bandwidth changes of 4 GHz and 8 GHz, respectively. The overall smaller sensitivity, compared to the single-ended case, indicates that the push-pull modulation scheme, with its inherent dynamic balance, offers improved resilience to certain fabrication errors.

In conclusion, the tolerance analysis confirms that both optimized designs maintain stable performance within typical fabrication error margins. The single-ended design is more sensitive to parameters governing the PPR (low-κ section), while the push-pull design demonstrates generally lower sensitivity and higher single-mode yield, enhancing its manufacturability.

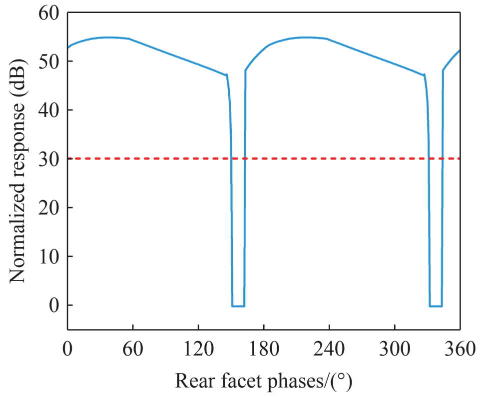

Fig. 21 Effect of random back-facet phase on the single-mode yield for push-pull modulation laser.

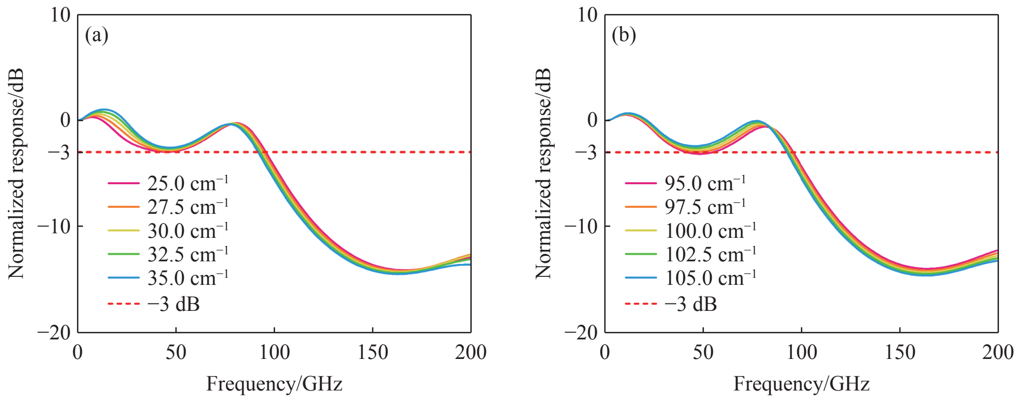

Fig. 22 Effect of fabrication variations on the small-signal response of the optimized push-pull modulation laser: (a) the κ_1-value of the low-κ and modulation sections and (b) the κ_2-value of the high-κ section.

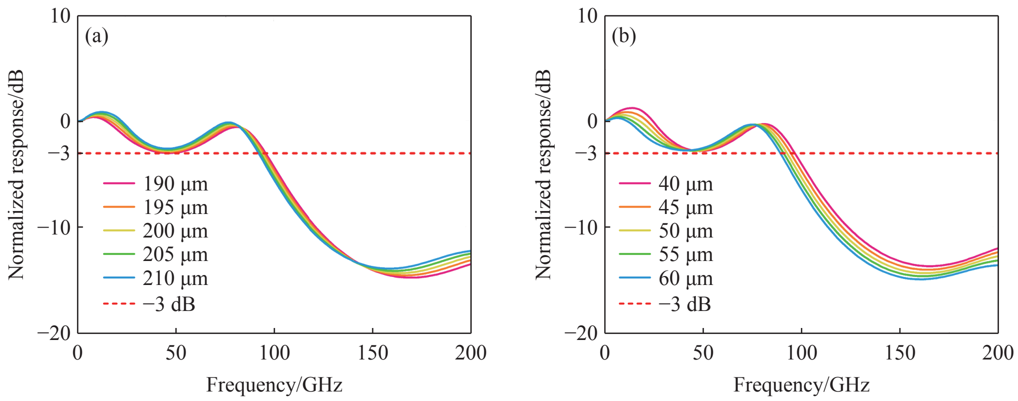

Fig. 23 Effect of fabrication variations on the small-signal response of the optimized push-pull modulation laser: (a) the length of the low-κ section and (b) the length of the modulation section.

7 Conclusion

In this work, we have systematically designed and numerically analyzed an IAL-based DFB laser incorporating a dual-κ grating, and evaluated its performance under both single-ended and push-pull modulation schemes. The proposed dual-κ grating design effectively addresses the uneven small-signal response typically associated with IAL structures, eliminating the need for complex butt-joint regrowth. Through optimization of the section lengths and coupling coefficients, the small-signal response and PPR frequency are effectively tailored.

In the single-ended modulated structure, the laser leverages three side modes to collectively excite the PPR effect, generating multiple resonance peaks that significantly extend the simulated small-signal modulation bandwidth to 185 GHz. In push-pull modulation, the optimized asymmetric design not only extends the bandwidth but also mitigates the characteristic low-frequency roll-off through the asymmetric cavity design, achieving a simulated small-signal modulation bandwidth of 94 GHz. Both modulation schemes support clear eye diagrams under 200 Gbit/s NRZ operation in simulation, with the push-pull modulated laser exhibiting a higher extinction ratio. Furthermore, tolerance analysis confirms that both designs maintain stable bandwidth under reasonable variations in coupling coefficients and section lengths, demonstrating good fabrication robustness.

In summary, the IAL-based dual-κ DFB laser appears to be a fabrication-friendly cavity-design approach for future high-speed short-reach optical interconnects, with flexibility in modulation scheme selection according to system requirements. Future work will focus on reducing the bias current and evaluating electro-thermal effects under more realistic device conditions.

8 Appendix: Simulation model

The optical cavity modes are calculated using the transfer-matrix method, which is well-suited for multisection laser simulations. The solution is iterated with a modified Newton's method until convergence is achieved. The model accounts for longitudinal inhomogeneities in carrier and photon distributions (i.e., spatial-hole-burning effects) and describes dynamic effects arising from coupling among multiple lasing modes [53-56]. Compared with time-domain total-field models such as VPIcomponentMaker, the mode-resolved approach implemented in LaserMatrix has been previously validated.

Following the established formalism of Feiste [54] and Wenzel et al. [55] for longitudinal field dynamics, we define the optical field vector comprising forward- and backward-propagating waves:

$$\mathbf{\Psi}(z,t)=\begin{pmatrix}\Psi^{+}\\ \Psi^{-}\end{pmatrix}\quad . \tag{1}$$

The traveling-wave equation satisfies

$$-i\frac{d\mathbf{\Psi}(z,t)}{dt}=\hat{\mathbf{H}}(z,t)\mathbf{\Psi}(z,t)\quad , \tag{2}$$

where $\hat{\mathbf{H}}(z,t)$ is matrix operator.

Equation (2) is solved under the following boundary conditions:

$$\begin{aligned}\Psi^{+}(0,t)&=r_0\Psi^{-}(0,t)\\ \Psi^{-}(L,t)&=r_L\Psi^{+}(L,t)\end{aligned}\quad , \tag{3}$$

where L is the cavity length and r_0 and r_L are the facet reflectivity values at z of 0 and L, respectively.

Expand the total field $\mathbf{\Psi}(z,t)$ through the cavity eigenmodes $\mathbf{\Phi}_n(z,t)$:

$$\mathbf{\Psi}(z,t)=\sum_n f_n(t)\mathbf{\Phi}_n(z,t)\quad , \tag{4}$$

where modes $\mathbf{\Phi}_n(z,t)$ are the solutions to the eigenvalue equation:

$$\hat{\mathbf{H}}(z,t)\mathbf{\Phi}_n(z,t)=\Omega_n(t)\mathbf{\Phi}_n(z,t)\quad . \tag{5}$$

the real part of the eigenvalue $\Omega_n(t)$ represents the mode angular frequency deviation from the reference angular frequency, while its imaginary part denotes the mode decay rate.

Through mode expansion of the traveling wave field (2) subject to boundary conditions, it is demonstrable that the modes are not power orthogonality.

The modes orthogonality condition is defined as:

$$\langle\mathbf{\Phi}_m|\mathbf{\Phi}_n\rangle=\int_0^L \Phi_m^{+}\cdot\Phi_n^{-}+\Phi_m^{-}\cdot\Phi_n^{+}dz=\delta_{m,n}\quad , \tag{6}$$

where $\delta_{m,n}$ is the Kronecker delta.

The scalar product in the Hilbert space is as follows:

$$\langle \boldsymbol{\Phi}_m | \boldsymbol{\Phi}_n^* \rangle = \int_0^L \Phi_m^+ \cdot \Phi_n^{+*} + \Phi_m^- \cdot \Phi_n^{-*} dz = \delta_{m,n} \quad . \quad (7)$$

For a deeper analysis, the total photon energy S, the stored reactive energy U of each mode, and the traveling wave energy V are expressed as:

$$S = \langle \boldsymbol{\Psi} | \boldsymbol{\Psi}^* \rangle = \int_0^L \left|\Psi^+\right|^2 + \left|\Psi^-\right|^2 dz \quad , \quad (8)$$

$$U = \langle \boldsymbol{\Psi} | \boldsymbol{\Psi} \rangle = \int_0^L 2\Psi^+\Psi^- dz \quad , \quad (9)$$

$$V = S - |U| \quad . \quad (10)$$

For every eigenmode $\boldsymbol{\Phi}$, the ratio of S to U provides

$$\frac{S}{|U|} = \frac{\langle \boldsymbol{\Phi} | \boldsymbol{\Phi}^* \rangle}{|\langle \boldsymbol{\Phi} | \boldsymbol{\Phi} \rangle|} = \frac{\int |\Psi^+|^2 + |\Psi^-|^2 dz}{\left|\int 2\Psi^+\Psi^- dz\right|} = \sqrt{K_z} \quad , \quad (11)$$

where K_z denotes the Petermann factor (or excess spontaneous emission factor).

The longitudinal confinement factor is written as:

$$\Gamma_z(N) = \frac{\langle \boldsymbol{\Phi} | \boldsymbol{\Phi}^* \rangle_{active}}{|\langle \boldsymbol{\Phi} | \boldsymbol{\Phi} \rangle|} \quad . \quad (12)$$

This factor, which is influenced by carrier variations, reflects the longitudinal distribution of the reactive photon density within the cavity.

To solve Equation (2) and analyze the modal dynamics, the optical field is expanded into time-dependent instantaneous modes [54]. This expansion yields a set of coupled-mode equations, which are solved alongside the rate equation for the longitudinal carrier distribution. For the eye diagram simulations, a fifth-order Runge-Kutta method is utilized, while the small-signal modulation response is derived from an analytical solution of the linearized equations.

References:

[1] TUCKER R S. High-speed modulation of semiconductor lasers[J]. *IEEE Transactions on Electron Devices*, 1985, 32(12): 2572-2584.

[2] LIU Z M, QIU CH, CHEN Y Y, *et al*.. Breaking bandwidth limits in high-speed directly modulated laser: synergistic strategies from conventional methods to cavity enhancement effects[J]. *Optics & Laser Technology*, 2025, 192: 113668.

[3] HUANG J O, LI CH, LU R G, *et al*.. Beyond the 100 Gbaud directly modulated laser for short reach applications[J]. *Journal of Semiconductors*, 2021, 42(4): 041306.

[4] ZAH C E, BHAT R, PATHAK B N, *et al*.. High-performance uncooled 1.3-μm $Al_xGa_yIn_{1-x-y}As/InP$ strained-layer quantum-well lasers for subscriber loop applications[J]. *IEEE Journal of Quantum Electronics*, 1994, 30(2): 511-523.

[5] PARILLAUD O, VAN DIJK F, VODJDANI N. Realization of 20 GHz directly modulated 1.55 μm DFB lasers using partially strain compensated quantum wells structures[C]. *International Conference on Indium Phosphide and Related Materials*, IEEE, 2005: 551-553.

[6] RALSTON J D, WEISSER S, ESQUIVIAS I, *et al*.. Control of differential gain, nonlinear gain and damping factor for high-speed application of GaAs-based MQW lasers[J]. *IEEE Journal of Quantum Electronics*, 1993, 29(6): 1648-1659.

[7] WEISSER S, LARKINS E C, CZOTSCHER K, *et al*. . 37 GHz direct modulation bandwidth in short-cavity InGaAs/GaAs MQW lasers with C-doped active regions[C]. *8th IEEE Lasers and Electro-Optics Society 1995 Annual Meeting*, IEEE, 1995: 91-92.

[8] UOMI K, AOKI M, TSUCHIYA T, *et al*.. Dependence of high-speed properties on the number of quantum wells in 1.55 μm InGaAs-InGaAsP MQW λ/4-shifted DFB lasers[J]. *IEEE Journal of Quantum Electronics*, 1993, 29(2): 355-360.

[9] WEISSER S, LARKINS E C, CZOTSCHER K, *et al*.. Damping-limited modulation bandwidths up to 40 GHz in undoped short-cavity $In_{0.35}Ga_{0.65}As$-GaAs multiple-quantum-well lasers[J]. *IEEE Photonics Technology Letters*, 1996, 8(5): 608-610.

[10] FUKAMACHI T, ADACHI K, SHINODA K, *et al*.. Wide temperature range operation of 25-Gb/s 1.3-μm InGaAlAs directly modulated lasers[J]. *IEEE Journal of Selected Topics in Quantum Electronics*, 2011, 17(5): 1138-1145.

[11] NAKAHARA K, SUGA K, OKAMOTO K, *et al*. . 112-Gb/s PAM-4 uncooled (25°C to 85°C) directly modulation of 1.3-μm InGaAlAs-MQW DFB BH lasers with record high bandwidth[C]. *45th European Conference on Optical*

Communication, IEEE, 2019: 1-3.

[12] SHINOHARA K, MIYAGOSHI R, SUZUKI Y, *et al.* . 106-Gbps PAM4 operation at an extinction ratio above 3.5 dB using a conventional buried-heterostructure directly modulated laser[C]. *2023 Optical Fiber Communications Conference and Exhibition*, IEEE, 2023: 1-3.

[13] DUMITRESCU M, TELKKÄLÄ J, KARINEN J, *et al.* . High-speed directly-modulated lasers with photon-photon resonance[C]. *23rd International Conference on Indium Phosphide and Related Materials*, IEEE, 2011: 1-4.

[14] WANG Y C, CHEN R Y, HSIEH P F, *et al.*. Phase-shifted distributed feedback lasers with two-layer moiré gratings[J]. *IEEE Photonics Technology Letters*, 2020, 32(11): 631-634.

[15] DOU ZH P, WANG J, SUN CH ZH, *et al.* . L-band directly-modulated distributed feedback lasers with low chirp and high extinction ratio[C]. *2024 Asia Communications and Photonics Conference (ACP) and International Conference on Information Photonics and Optical Communications*, IEEE, 2024: 1-3.

[16] NAKAHARA K, WAKAYAMA Y, KITATANI T, *et al.*. Direct modulation at 56 and 50 Gb/s of 1.3-μm InGaAlAs ridge-shaped-BH DFB lasers[J]. *IEEE Photonics Technology Letters*, 2015, 27(5): 534-536.

[17] MATSUI Y, PHAM T, SUDO T, *et al.*. 28-gbaud PAM4 and 56-Gb/s NRZ performance comparison using 1310-nm Al-BH DFB laser[J]. *Journal of Lightwave Technology*, 2016, 34(11): 2677-2683.

[18] KJEBON O, SCHATZ R, LOURDUDOSS S, *et al.*. Modulation response measurements and evaluation of MQW InGaAsP lasers of various designs[J]. *Proceedings of the SPIE*, 1996, 2684: 138-152.

[19] MATSUI Y. *Directly modulated laser technology: past, present, and future*[M]//CHANG F. Datacenter Connectivity Technologies. New York: River Publishers, 2017: 87-171.

[20] KJEBON O, SCHATZ R, CARLSSON C, *et al.* . Experimental evaluation of detuned loading effects on distortion in edge emitting DBR lasers[C]. *2002 International Topical Meeting on Microwave Photonics*, IEEE, 2002: 125-128.

[21] MORTHIER G, SCHATZ R, KJEBON O. Extended modulation bandwidth of dbr and external cavity lasers by utilizing a cavity resonance for equalization[J]. *IEEE Journal of Quantum Electronics*, 2000, 36(12): 1468-1475.

[22] MATSUI Y, SCHATZ R, PHAM T, *et al.*. 55 GHz bandwidth distributed reflector laser[J]. *Journal of Lightwave Technology*, 2017, 35(3): 397-403.

[23] RAJESWARI G V, MOEHRLE M, SIGMUND A, *et al.* . Record 4 × 106 gbps transmission from a directly modulated laser array using photon-photon resonance[C]. *2025 Optical Fiber Communications Conference and Exhibition*, IEEE, 2025: 1-3.

[24] TROPPENZ U, KREISSL J, MÖHRLE M, *et al.*. 40 Gbit/s directly modulated lasers: physics and application[J]. *Proceedings of SPIE*, 2011, 7953: 79530F.

[25] PANG X D, SALGALS T, LOUCHET H, *et al.*. 200 Gb/s optical-amplifier-free IM/DD transmissions using a directly modulated O-band DFB+R laser targeting LR applications[J]. *Journal of Lightwave Technology*, 2023, 41(11): 3635-3641.

[26] CHE D, MATSUI Y, SCHATZ R, *et al.*. 200-Gb/s direct modulation of a 50-GHz class laser with advanced digital modulations[J]. *Journal of Lightwave Technology*, 2021, 39(3): 845-852.

[27] MAO Y F, REN ZH L, LU G, *et al.*. Modulation bandwidth enhancement in distributed reflector laser based on identical active layer approach[J]. *IEEE Photonics Journal*, 2018, 10(3): 1502308.

[28] BAN D CH, CHEN J, JIN Y, *et al.*. Demonstration of a directly modulated laser achieving bandwidth exceeding 50 GHz with an integrated active feedback waveguide[J]. *Photonics Research*, 2024, 12(12): 2855-2862.

[29] MA X, QI H F, DING Y D, *et al.*. Demonstration of a three-active-section DFB laser with photon-photon resonance and detuned loading effects to obtain enhanced bandwidth and maintained high output power[J]. *Optics & Laser Technology*, 2025, 182: 112127.

[30] DOU ZH P, WANG J, SUN CH ZH, *et al.*. A compound-cavity distributed feedback laser with bandwidth over 50 GHz based on uniform gratings[J]. *IEEE Photonics Technology Letters*, 2024, 36(24): 1437-1440.

[31] DOU ZH P, WANG J, SUN CH ZH, *et al.* . A dual-segment distributed feedback laser with 70 GHz bandwidth[C]. *2024 Asia Communications and Photonics Conference (ACP) and International Conference on Information Photonics and Optical Communications*, IEEE, 2024: 1-3.

[32] REN M H, LIU Z Q, JIA SH H, *et al.*. C-band 33-GHz high flatness photon-photon resonance directly modulated semiconductor lasers[J]. *Optics Express*, 2025, 33(22): 45525-45538.

[33] QI J Q, XI Y P, LI X. Enhanced modulation bandwidth by exploiting photon resonance in push-pull modulated DFB lasers[C]. *2015 International Conference on Numerical Simulation of Optoelectronic Devices*, IEEE, 2015: 127-128.

[34] MONTROSSET I, BARDELLA P. Laser dynamics providing enhanced-modulation bandwidth[C]. *Proceedings of SPIE*, 2014, 9134: 91340H.

[35] MONTROSSET I, BARDELLA P. Design and simulation of quantum-dot-based push-pull DFB lasers[C]. *Proceedings of SPIE*, 2018, 10526: 1052605.

[36] CHEN J Y, MACIEJKO R, MAKINO T. Dynamic properties of push-pull DFB semiconductor laser[J]. *IEEE Journal of Quantum Electronics*, 1996, 32(12): 2156-2165.

[37] NOWELL M C, CARROLL J E. Push-pull modulated DFB lasers with low chirp and enhanced cut-off frequency for high speed systems[C]. *IEE Colloquium on High Capacity Optical Communications*, IET, 1994: 5/1-5/6.

[38] MARCENAC D, NOWELL M C, CARROLL J E. Theory of enhanced AM-modulation bandwidth in Push-pull DFB lasers[C]. *Proceedings of LEOS'94*, IEEE, 1994: 163-164.

[39] FLANIGAN B J, CARROLL J E, NOWELL M C, *et al*.. Improved resonance and chirp mechanisms for multigigabit/s push-pull modulated DFB lasers[J]. *IEE Proceedings – Optoelectronics*, 1996, 143(1): 49-56.

[40] NOWELL M C, CARROLL J E, ZHANG L M. Push-pull multi-gigabit/s modulated DFB lasers with tow chirp and high cut-off frequency[C]. *Proceedings of Conference on Lasers and Electro-Optics*, Optica Publishing Group, 1994: CWJ1.

[41] MARCENAC D D, NOWELL M C, CARROLL J E. Theory of enhanced amplitude modulation bandwidth in push-pull modulated DFB lasers[J]. *IEEE Photonics Technology Letters*, 1994, 6(11): 1309-1311.

[42] CHI J W, LI X, NIU CH N, *et al*.. Enhanced modulation bandwidth by delayed push-pull modulated DFB lasers[J]. *Micromachines*, 2023, 14(3): 633.

[43] CHI J W, LI X, NIU CH N, *et al*.. Output optical power enhancement of push-pull modulated DFB laser with asymmetric structure[J]. *IEEE Photonics Journal*, 2023, 15(5): 1502208.

[44] BAN D CH, WANG J, WANG X, *et al*.. Improvement on stability of direct modulation laser with integrated active feedback by partial corrugated gratings[J]. *Optics Express*, 2023, 31(18): 28778-28791.

[45] BARDELLA P, MONTROSSET I. A new design procedure for dbr lasers exploiting the photon-photon resonance to achieve extended modulation bandwidth[J]. *IEEE Journal of Selected Topics in Quantum Electronics*, 2013, 19(4): 1502408.

[46] MATSUI Y. Two-kappa DBR laser: US, US11233375B2[P]. 2022-01-25.

[47] NOWELL M C, ZHANG L M, CARROLL J E, *et al*.. Chirp reduction using push-pull modulation of three-contact lasers[J]. *IEEE Photonics Technology Letters*, 1993, 5(12): 1368-1371.

[48] ZOZULIA A, SCHATZ R, RIHANI S, *et al*.. C-band directly modulated lasers with tunable photon-photon resonance in InP membrane[J]. *IEEE Journal of Quantum Electronics*, 2024, 60(6): 2200312.

[49] CHACIŃSKI M G, SCHATZ R, ISAKSSON M, *et al*.. Effects of detuned loading on the modulation performance of widely tunable MG-Y lasers[J]. *Proceedings of SPIE*, 2008, 6997: 699709.

[50] CHACIŃSKI M, SCHATZ R. Impact of losses in the Bragg section on the dynamics of detuned loaded DBR lasers[J]. *IEEE Journal of Quantum Electronics*, 2010, 46(9): 1360-1367.

[51] MATSUI Y, SCHATZ R, CHE D, *et al*.. Low-chirp isolator-free 65-GHz-bandwidth directly modulated lasers[J]. *Nature Photonics*, 2021, 15(1): 59-63.

[52] LIU Z M, SCHATZ R, QIU C, *et al*.. High-speed directly modulated partial corrugated grating distributed feedback laser with multiple photon-photon resonances[J]. *Proceedings of SPIE*, 2025, 13990: 1399009.

[53] SCHATZ R. Dynamics of spatial hole burning effects in DFB lasers[J]. *IEEE Journal of Quantum Electronics*, 1995, 31(11): 1981-1993.

[54] FEISTE U. Optimization of modulation bandwidth in DBR lasers with detuned Bragg reflectors[J]. *IEEE Journal of Quantum Electronics*, 1998, 34(12): 2371-2379.

[55] WENZEL H, BANDELOW U, WUNSCHE H J, *et al*.. Mechanisms of fast self pulsations in two-section DFB lasers[J]. *IEEE Journal of Quantum Electronics*, 1996, 32(1): 69-78.

[56] BJORK G, NILSSON O. A new exact and efficient numerical matrix theory of complicated laser structures: properties of asymmetric phase-shifted DFB lasers[J]. *Journal of Lightwave Technology*, 1987, 5(1): 140-146.

Author Biographies：

LIU Zi-ming (1998—) is currently a Ph.D. candidate at Changchun Institute of Optics, Fine Mechanics and Physics, Chinese Academy of Sciences, and is jointly trained at the Pengcheng Laboratory. His research interests include the development of high–speed directly modulated lasers and hybrid external–cavity lasers. E-mail: liuziming98@163.com

SCHATZ Richard (1963—) received the Ph.D. degree from the Royal Institute of Technology (KTH), Stockholm, Sweden, in 1995. His research is focused on the modeling, design, and characterization of fiber–optical transmitters (edge emitter lasers, quantum cascade lasers, VCSELs, and modulators), both for on–off keying and multilevel modulation formats. E-mail: rschatz@kth.se

QIU Cheng (1984—) received the Ph.D. degree from Changchun Institute of Optics, Fine Mechanics and Physics, Chinese Academy of Sciences, in 2019. His current research interests include wide range tunable laser source, optical networks on chips, optical field tuning on photonics active device, inverse design of passive and active photonic devices. E-mail: qiucheng@ciomp.ac.cn

ZHANG Nan (1984—) received the Ph.D. degree in condensed matter physics from the Changchun Institute of Optics, Fine Mechanics and Physics, Chinese Academy of Sciences, in 2014. His research interests include high–speed electro–optic modulators, semiconductor lasers, and photonic integration, as well as silicon–based optoelectronic heterogeneous integration and device physics. E-mail: zhangn06@pcl.ac.cn